On the importance of electron-electron and electron-phonon scatterings and energy renormalizations during carrier relaxation in monolayer transition-metal dichalcogenides

Jörg Hader,[1, a)] Josefine Neuhaus,[2] Jerome V. Moloney,[1] and Stephan W. Koch[2]
[1)] *Wyant College of Optical Sciences, University of Arizona, 1630 E. University Blvd., Tucson, Arizona 85721, USA*
[2)] *Department of Physics and Material Sciences Center, Philipps-University Marburg, Renthof 5, 35032 Marburg, Germany*

(Dated: 14 June 2022)

An *ab initio* based fully microscopic many-body approach is used to study the carrier relaxation dynamics in monolayer transition-metal dichalcogenides. Bandstructures and wavefunctions as well as phonon energies and coupling matrix elements are calculated using density functional theory. The resulting dipole and Coulomb matrix elements are implemented in the Dirac-Bloch equations to calculate carrier-carrier and carrier-phonon scatterings throughout the whole Brillouin zone. It is shown that carrier scatterings lead to a relaxation into hot quasi-Fermi distributions on a single femtosecond timescale. Carrier cool down and inter-valley transitions are mediated by phonon scatterings on a picosecond timescale. Strong, density-dependent energy renormalizations are shown to be valley-dependent. For $MoTe_2$, $MoSe_2$ and MoS_2 the change of energies with occupation is found to be about 50% stronger in the Σ and Λ side valleys than in the K and K' valleys. However, for realistic carrier densities, the materials always maintain their direct bandgap at the K points of the Brillouin zone.

I. INTRODUCTION

Monolayer transition-metal dichalcogenides (TMDCs) have a variety of properties that make them very interesting for applications in opto-electronic devices. Two of the most important characteristics are their direct bandgap and the exceptionally strong Coulomb interaction due to inefficient screening outside the monolayer plane. The highly efficient optical coupling leads to a near-bandgap absorption of up to 10-20% from a single layer[1,2] which makes the material attractive for applications like photo-detectors[3–5] or solar cells[6,7]. The prominent optical coupling also leads to strong luminescence and, consequently, promising performance as light-emitting diodes[8–10]. Monolayer TMDCs have also been shown to be able to provide strong optical gain[11,12] which enables them to be used as active material in lasers[13–15].

The strong Coulomb interaction also enables the possibility to tune the bandgap over a wide spectral range. Injecting carriers into the system leads to energy renormalizations on the order of the exciton binding energy which in these materials is of the order of hundreds of meV[16–19]. Fig.1 gives an example for the energy renormalizations in a monolayer of $MoTe_2$. Here, equal electron and hole densities of $12.5\times10^{12}/\mathrm{cm}^2$ were placed in Fermi dstributions at 300 K. Figs.1 (a) and (b) show the carrier distributions in the band that is energetically closest to the bandgap at the K-point (A-band). Mirroring these results along the Γ-M line gives the results for the B-band which has the opposite spin and the same gap at K' as the A-band at K. As can be seen from Fig.1 (c), the presence of the quasi-equilibrium carriers reduces the bandgap by about 100 meV throughout the whole Brillouin zone (BZ). The renormalization is strongly enhanced in the vicinity of high carrier occupations, reaching over 260 meV at the K-point.

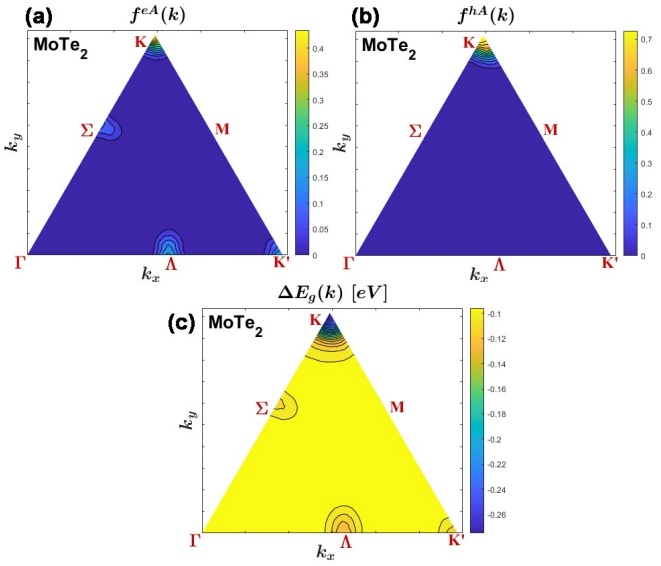

FIG. 1. (a)/(b): Electron/hole occupations of the A-band for a total electron/hole density of $12.5\times10^{12}/\mathrm{cm}^2$ in a monolayer $MoTe_2$. Carriers are assumed to be in thermal equilibrium Fermi distributions at 300 K. (c): renormalization of the A-bandgap in the presence of the carriers.

The strong energy renormalizations open the interesting possibility to tune the operating wavelength through

[a)] Author to whom correspondence should be addressed: jhader@acms.arizona.edu

controlled carrier injection. Also, the energetic order of the valleys could potentially be changed, e.g., by exciting resonantly with a specific valley transition and/or using polarized, spin-valley sensitive excitation[20,21]. However, valley specific renormalizations require non-thermal carrier distributions. Once pump injected carriers have thermalized into Fermi distributions with a global Fermi level throughout the BZ, the energies of individual valleys will only be determined by the total carrier density. A potential drawback of the density dependent renormalizations was pointed out in Refs.[11,22]. If the energies of a side valley of the electron A-band renormalize faster with increasing carrier density than the energy at the direct bandgap at K, it could potentially happen that the side valley is lowered below the K-valley and the material becomes optically indirect. In thi case, the pump injected electrons would predominantly occupy the side valley, and, since the hole bandstructure does not have side valleys, electrons in them are not available to recombine optically. This will degrade the material's performance for applications like light emitting diodes or lasers. As we will show here, whether such a transition will occur strongly depends on details of the bandstructure.

Valley- and excitation-dependent renormalizations for carriers in static thermal equilibrium distributions were discussed in Ref.[22] using similar first principles based microscopic models as we employ here. In Ref.[23] a similar model was extended in order to be able to study the nonequilibrium carrier relaxation due to electron-electron scatterings. However, inter-valley carrier transitions involve large momentum transfer which is predominantly mediated by scatterings involving optical and acoustical phonons. These were not included in Ref.[23]. The influence of phonon-assisted inter- and intra-valley scatterings were investigated in Refs.[24–26], but only for carriers in equilibrium distributions. In Ref.[12] electron-electron and electron-phonon scatterings were included to study nonequilibrium carrier relaxation. However, that investigation was limited to intra-valley dynamics using a simplified one-dimensional bandstructure model.

Here, we employ a fully microscopic many-body model that includes electron-electron and electron-phonon scatterings throughout the full BZ. The model is based on input from first principle density functional theory (DFT) for bandstructures, electron wavefunctions and phonon energies and coupling matrix elements. The model is used to determine timescales for the relaxation of carriers that are excited above the bandgap. It also yields times for inter-valley and intra-valley scatterings that lead to global quasi equilibrium distributions as well as for the subsequent cool-down to the ambient temperature by removal of excess energy via phonon emission.

Details of the model are outlined in Sec.II where we will also show results of the DFT calculations. Results of the many-body model are discussed in Sec.III for monolayer $MoTe_2$, $MoSe_2$ and MoS_2. In Sec.III A we present numerical results assuming an artificial static carrier distribution to initialize the system in order to be able to clearly distinguish between the excitation related dynamics and the subsequent carrier relaxation. Carrier scattering processes are turned on after the initialization. In Sec.III A 1 we examine the case of an initial distribution that is energetically located above the barriers separating different bandstructure valleys. We determine the characteristic carrier relaxation times and show the influence of electron-electron scatterings versus electron-phonon scatterings due to optical and acoustical phonons at various stages of the relaxation process. In Sec.III A 2 we present results where we assume excitation at the bandgap in the K-valley and investigate the subsequent carrier transfer to the K', Σ and Λ valleys. After that, in Sec.III B, we simulate the situation where the system is excited dynamically using a 50 fs optical pulse which allows us to identify characteristic details of the relaxation dynamics might be observable in the experiment. Finally, in Sec.III C, we investigate the energy renormalizations after full carrier thermalisation for various excitation levels in order to see if a transition from direct to indirect bandgap occurs. We summarize our results in Sec.IV.

II. THEORETICAL MODELS

The theoretical approach used here is based on the Dirac-Bloch equations (DBE) as described in Ref.[12] and references therein. The DBE are the equations of motions for the microscopic polarizations, $p_{\mathbf{k}i}$, and the occupation probabilities for electrons/holes, $f^{e/h}_{\mathbf{k}i}$:

$$i\hbar\frac{d}{dt}p_{\mathbf{k}i} = \left(\varepsilon^{e}_{\mathbf{k}i} - \varepsilon^{h}_{\mathbf{k}i}\right)p_{\mathbf{k}i} - \left(1 - f^{e}_{\mathbf{k}i} - f^{h}_{\mathbf{k}i}\right)\Omega_{\mathbf{k}i} + i\hbar\left.\frac{d}{dt}p_{\mathbf{k}i}\right|_{\text{corr}}, \tag{1}$$

$$\frac{d}{dt}f^{e/h}_{\mathbf{k}i} = -\frac{2}{\hbar}\,\text{Im}\left(\Omega_{\mathbf{k}i}p^{*}_{\mathbf{k}i}\right) + \left.\frac{d}{dt}f^{e/h}_{\mathbf{k}i}\right|_{\text{corr}}. \tag{2}$$

Here, Ω are the renormalized Rabi frequencies

$$\Omega_{\mathbf{k}i} = \frac{e}{m_0 c}\mathbf{A}\cdot\boldsymbol{\mu}_{\mathbf{k}i} - \sum_{\mathbf{k}'}V^{ehhh}_{\mathbf{k}-\mathbf{k}';\mathbf{k}';\mathbf{k}}(f^{e}_{\mathbf{k}'i} - f^{h}_{\mathbf{k}'i}) - \sum_{\mathbf{k}'}\left[V^{ehhe}_{\mathbf{k}-\mathbf{k}';\mathbf{k}';\mathbf{k}}p_{\mathbf{k}'i} + V^{eehh}_{\mathbf{k}-\mathbf{k}';\mathbf{k}';\mathbf{k}}p^{*}_{\mathbf{k}'i}\right], \tag{3}$$

where $\boldsymbol{\mu}_{\mathbf{k}i}$ are the dipole matrix elements between the electron and hole bands with band index i and momentum $\mathbf{k}$, and ε are the renormalized energies:

$$\varepsilon^{e/h}_{\mathbf{k}i} = \epsilon^{e/h}_{\mathbf{k}i} - \sum_{\mathbf{k}'}\left[V^{eeee/hhhh}_{\mathbf{k}-\mathbf{k}';\mathbf{k}';\mathbf{k}} - V^{eheh/hehe}_{\mathbf{k}-\mathbf{k}';\mathbf{k}';\mathbf{k}}\right]f^{e/h}_{\mathbf{k}'i} + \sum_{\mathbf{k}'}\left[V^{ehee/hhhe}_{\mathbf{k}-\mathbf{k}';\mathbf{k}';\mathbf{k}}p_{\mathbf{k}'i} + c.c.\right]. \tag{4}$$

Coulomb matrix elements of the type V^{ehhh} in Eq.(3) and $V^{ehee/hhhe}$ in Eq.(4) mediate Auger-like processes. Coulomb terms of the type V^{eehh} in Eq.(3) and

$V^{eheh/hehe}$ in Eq. (4) represent pair creation and annihilation processes. Whereas these processes can be neglected in systems with weaker Coulomb interaction, like III-V semiconductors, they are important in TMDCs. Here, they lead to a non-trivial ground state deviating from the case of zero occupations and polarizations. The dominant influence of these terms is to contribute to a renormalisation of the hole bands which we take into account by calculating the so-called Coulomb hole. We have tested that these Auger- and pair-processes have a negligible impact on the carrier dynamics and can be neglected there.

The term involving V^{ehhe} in Eq. (3) represents the renormalisation of the optical coupling as known from the classical semiconductor Bloch equations (SBE). It leads to the generation of bound excitonic states below the bandgap and to the Coulomb-enhancement of the continuum absorption. As in the SBE, the term involving $V^{eeee/hhhh}$ in Eq. (4) leads to the exitation dependent energy renormalisation that we will investigate in detail here.

The terms marked $|_{corr}$ summarize many-body correlations beyond the Hartree-Fock level. They contain carrier scatterings due to electron-electron and electron-phonon interactions. The higher order correlations are also responsible for the plasma-screening of the Coulomb interaction. In monolayer TMDCs, the correct inclusion of these higher order terms is of particular importance due to the exceptional strength of the Coulomb interaction. We treat these terms and the resulting screening as outlined in Ref.[12].

For the calculations as shown here, scatterings are only taken into account explicitly for the carrier distributions. Polarizations are only included for the optical excitation of carriers. Since our focus is on the subsequent incoherent dynamics of the distributions and not details of the excitation, we approximate the scatterings that lead to the dephasing of the polarisations by a simple dephasing rate.

The electron-electron scattering equations solved here are outlined in Ref.[12]. Whereas in that reference only one branch of dispersionless optical phonons was taken into account for the electron-phonon scattering, here, we include all optical and acoustical phonon branches. The generalized electron-phonon scattering equations take the form:

$$\begin{aligned}\frac{d}{dt}f_{\mathbf{k}i}\Big|^{\text{ph.}}_{\text{corr.}} &= \frac{2\pi}{\hbar}\sum_{\mathbf{q},m} g^{i,m}_{\mathbf{k};\mathbf{q}}\tilde{g}^{i,m}_{\mathbf{k};\mathbf{q};\mathbf{k}+\mathbf{q}}\mathcal{D}\left(\tilde{\varepsilon}_{\mathbf{k}+\mathbf{q}i}-\tilde{\varepsilon}_{\mathbf{k}i}-\hbar\omega^m_{\mathbf{q}}\right)\\ &\quad\times\left[(n^m_{\mathbf{q}}+1)f_{\mathbf{k}+\mathbf{q}i}\bar{f}_{\mathbf{k}i}-n^m_{\mathbf{q}}f_{\mathbf{k}i}\bar{f}_{\mathbf{k}+\mathbf{q}i}\right]\\ &+\frac{2\pi}{\hbar}\sum_{\mathbf{q},m} g^{i,m}_{\mathbf{k};\mathbf{q}}\tilde{g}^{i,m}_{\mathbf{k};\mathbf{q};\mathbf{k}}\mathcal{D}\left(\tilde{\varepsilon}_{\mathbf{k}-\mathbf{q}i}-\tilde{\varepsilon}_{\mathbf{k}i}-\hbar\omega^m_{\mathbf{q}}\right)\\ &\quad\times\left[n^m_{\mathbf{q}}f_{\mathbf{k}-\mathbf{q}i}\bar{f}_{\mathbf{k}i}-(1+n^m_{\mathbf{q}})f_{\mathbf{k}i}\bar{f}_{\mathbf{k}-\mathbf{q}i}\right], \quad (5)\end{aligned}$$

where we use the abbreviation $\bar{f}$ for $(1-f)$ and combined the band indices i with the electron/hole index e/h. $\pi\mathcal{D}(x)=\frac{\eta}{x^2+\eta^2}$ denotes the numerical energy-conserving function, where we include a phenomenological broadening of $\eta = 50\,\text{meV}$. Numerical tests showed that the exact value of this broadening was insignificant for the final results. The renormalized transition energies $\tilde{\varepsilon}$ are calculated as in Eq.(4) but with Coulomb matrix elements which include plasma-screening due to excited carriers in addition to the screening from the dielectric environment which is already included in the matrix elements V. The index m labels the nine phonon branches[39,40], all of which are taken into account in our numerical evaluations. The phonon energies are denoted by $\hbar\omega^m_{\mathbf{q}}$. $n^m_{\mathbf{q}}$ are the phonon occupation numbers. The quantities g and $\tilde{g}$ are the unscreened and screened phonon coupling matrix elements, respectively. The additional $\mathbf{k}$-index on the phonon coupling matrix elements arises from the fact that the momentum dependence of the electron wavefunctions is included explicitly here while the studies in Ref.[12] exclusively focused on the K-valley and used the electron wavefunctions at this point only.

In Eq.(5), the first term of the second line corresponds to scattering of carriers into the state $\mathbf{k}, i$ via phonon emission and the second term represents out-scattering via phonon absorption. The first term of the fourth line represents in-scattering via phonon absorption and the last term out-scattering via phonon emission. For all processes the initial state has to be occupied, i.e. the occupation f has to be non-zero, and the final state has to be at least partially empty, $(1-f)>0$. Energy has to be conserved and the scattering probability is given by the phonon coupling matrix elements g.

The unrenormalized single-particle energies, ϵ, are calculated via DFT using the Vienna *ab initio* simulation package (VASP)[27–31]. Details of these calculations are described in Ref.[12] for $MoTe_2$ and executed analogously for the other materials. Besides the bandstructures, we also extract the dipole matrix elements and the wavefunctions needed to evaluate the Coulomb matrix elements from these calculations. The full k-dependence throughout the BZ is taken into account in all calculations for the single particle energies and dipole matrix elements. Unlike in Ref.[12], no simplification in terms of a massive Dirac fermion model with fitted bands is used. For the Coulomb matrix elements we evaluate the wavefunction-dependent form factors only in the vicinity of the K and Σ point and assume the same factors for the K' and Λ valleys. In regions away from these points the form factor of the nearest valley is used.

For all materials investigated here, the bandstructure has the same basic features. As representative example, Fig.2 shows the calculated unrenormalized electron and hole bands for the case of a monolayer of $MoTe_2$. The lowest two electron bands and highest two hole bands are related through time reversal symmetry. Spin-orbit splitting lifts the degeneracy of the bands with opposite spin at K and K'. The electron band with the lowest energy at K and the hole band with the highest energy at K are referred to as the A-bands. Carriers in the so-called B-band have the opposite spin from those in the A-

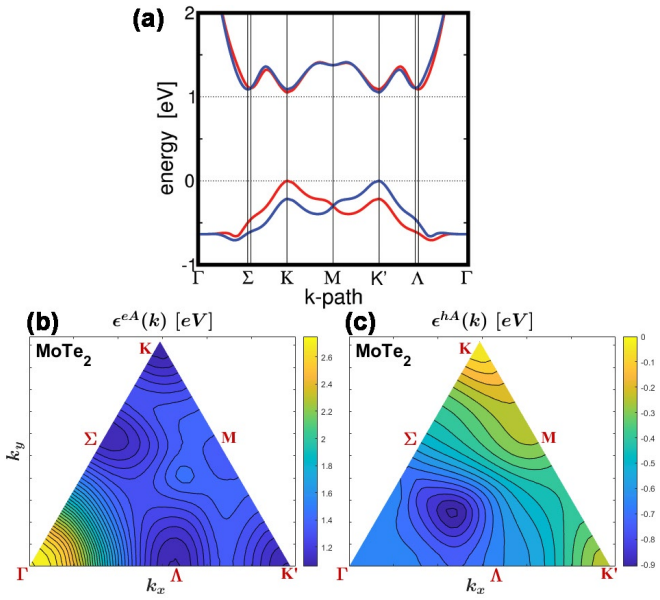

FIG. 2. (a): lowest two electron and highest two hole bands in a monolayer of $MoTe_2$ along a one-dimensional path through the BZ. Red/blue: bands for carriers with spin up/down (A/B-band). Bottom: energy of the electron (b) and hole (c) A-bands in the irreducible sector of the BZ. Spacing between contour lines is 50 meV.

TABLE I. Calculated unrenormalized energies in the electron A-band at critical points of the BZ and at energy maxima, $m_{P;P'}$, between points P and P'. Energies in [eV].

	K	K'	Λ	Σ	$m_{K;\Sigma}$	$m_{K';\Lambda}$	$m_{K;K'}$
$MoTe_2$	1.058	1.093	1.091	1.108	1.323	1.363	1.410
$MoSe_2$	1.446	1.468	1.496	1.474	1.769	1.784	1.900
MoS_2	1.708	1.711	1.821	1.892	2.156	2.160	2.309

band. Energies of the B-band can be derived from those of the A-band by mirroring perpendicular to the $\Gamma-M$ line. For excitation with linear polarized light the the physics within the A-band at K is the same as that within the B-band at K'. Thus, we reduce our presentations to the the A-band in the following.

There are three additional minima in the electron A-band structure at K', Σ and Λ. The hole A-band has maxima at the K- and K'-points and, additionally, a local maximum at the Γ-point. The energies of the unrenormalized electron A-bands at critical points of the BZ are listed for all materials investigated here in Table I. Hole energies in the A-band are listed in Table II.

It should be noted that the exact valley energies are very sensitive to details of the DFT calculation. In turn, the excitation dependent energy renormalizations that will be studied in Sec.III C are strongly influenced by the exact separations between main and side valleys. One major aspect concerning the offset between the different valleys is the lattice constant. Already differences of one percent in the lattice constant change the

TABLE II. Calculated unrenormalized energies in the hole A-band at K, K' and Γ and at energy minima, $m_{P;P'}$, between points P and P'. Energies in [eV].

	K	K'	Γ	$m_{K;K'}$	$m_{K;\Gamma}$	$m_{K';\Gamma}$
$MoTe_2$	0.000	-0.214	-0.393	-0.633	-0.656	-0.705
$MoSe_2$	0.000	-0.183	-0.670	-0.435	-0.777	-0.853
MoS_2	0.000	-0.146	-0.153	-0.706	-0.838	-0.919

calculated DFT bandgap in the range of 100 meV and may result in the transition from a direct to an indirect semiconductor.[32–34]. In order to be as precise as possible, we included van-der-Waals interaction via Grimme's dispersion correction, resulting in relaxed in-plane lattice constants of 3.50Å for $MoTe_2$, 3.28Å for $MoSe_2$, and 3.15Å for MoS_2, which is comparable to experimental findings.[38] Based on these parameters, we find a direct bandgap at K for all materials investigated here and a separation from the side valleys at Σ and Λ that exceeds the room temperature thermal energy of about 26 meV.

Phonon energies and coupling matrix elements are calculated using the DFT software Quantum Espresso[36,37]. For the non-collinear Kohn-Sham wavefunctions with spin-orbit coupling, the plane-wave basis set with a 49 Rydberg energy cut-off, Perdew-Burke-Ernzerhof type generalized gradient approximated exchange-correlation functional, and projector augmented wave (PAW) method with full-relativistic potentials were used. The resulting phonon dispersions were found in good agreement with the literature (see e.g. Refs.[39,40]). The full **k**- and **q**-dependence of the phonon dispersions and coupling matrix elements are taken into account in all calculations.

III. RESULTS

In the following we examine results for monolayers of $MoTe_2$, $MoSe_2$ and MoS_2 suspended on a SiO_2 substrate and at a temperature of 300 K. In all studies of the dynamics only the lowest two electron and highest two hole bands – A and B – are included. Excitation with linear polarized light is assumed which creates equal amounts of carriers at the K and K' points in bands of opposite spin.

A. Artificial Excitation

Here, we initialize the carrier distributions with an artificial, static distribution that allows to clearly determine timescales in the subsequent relaxation as well as the importance of various scattering processes within it. The initial distributions are given by the formula:

$$f_{\mathbf{k}i} = \frac{f_0 \mu^2_{\mathbf{k}i}}{\mu^2_{max}} \exp\left(-\frac{1}{2}\left(\frac{\epsilon^e_{\mathbf{k}i} - \epsilon^h_{\mathbf{k}i} - \hbar\omega_L}{\Delta}\right)^2\right), \qquad (6)$$

where $\mathbf{k}$ is the two-dimensional momentum vector, i is the band index and $\epsilon^{e/h}$ are the unrenormalized electron/hole energies. These distributions approximate a case where carriers are optically excited at an energy $\hbar\omega_L$ and form a Gaussian distribution of width Δ. The occupation probabilities are weighted with the square of the dipole matrix element $\mu_{\mathbf{k}i}$ between the i'th electron and hole band assuming a vanishing optical coupling between states with unequal spin. μ_{max} is the largest dipole matrix element between any states. For all cases studied here, a broadening $\Delta = 66\,\text{meV}$ is used.

1. Above Bandgap Excitation

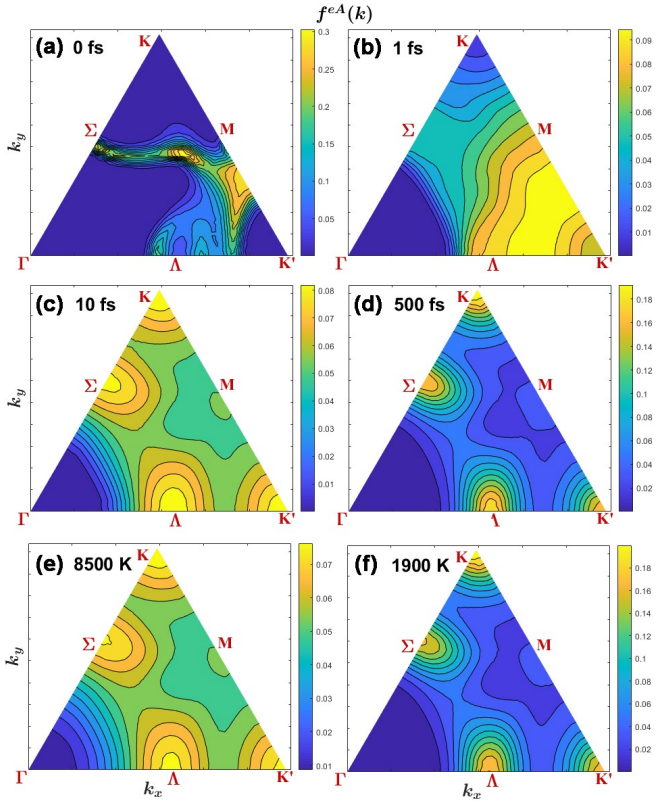

FIG. 3. (a), (b), (c), (d): Occupations of the electron A-band in a monolayer $MoTe_2$ at various times after initialisation according to Eq.(6) with $f_0 = 1.28$. Labels give the time after the start of relaxation. (e), (f): Occupation of the electron A-band for the same total electron density as in (a)-(d), but using Fermi distributions with carrier temperatures of 8500 K and 1900 K, respectively.

Fig.3 (a) shows the distributions created in the electron A-band using Eq.(6) for an excitation energy $\hbar\omega_L$ 800 meV above the unrenormalized bandgap. Here, a scaling $f_0 = 1.28$ was used which leads to a total electron sheet carrier density of about $1 \times 10^{14}/\text{cm}^2$. Figs.3 (b), (c), and (d) show the distributions after 1 fs, 10 fs, and 500 fs of relaxation, respectively. As can be seen in Fig. 3 (b), carrier scatterings broaden the distribution dramatically on a single femtosecond timescale. The excitation high above the bandgap is ideal for fast relaxation. Initial states are highly occupied and final states at lower energies are mostly empty which eliminates slow down of the relaxation due to phase space filling in this initial phase. Also, carriers located in rather narrow momentum regions at high energies screen the Coulomb interaction far less efficiently than if the same amount of carriers are relaxed and distributed throughout wide regions of the BZ.

After only 10 fs the carriers have relaxed to the bottom of the band and assume Fermi-like distributions with maximum occupation at minimum energy (see Fig.3 (c)). The excess energy from the excitation leads to very hot distributions. Using Fermi distributions for the same electron density we find a very good match to the distribution after 10 fs assuming a carrier temperature of 8,500 K (see Fig.3 (e)). The carriers subsequently cool down due to phonon emission. As can be seen from Figs.3 (d) and (f), after 500 fs the distribution can be matched assuming a carrier temperature of 1,900 K. Subsequently, the carriers cool down further toward the lattice temperature of 300 K on a picosecond timescale.

Fig.4 shows the individual contributions of electron-electron scatterings and of electron-phonon scatterings to the carrier relaxation at the start of the relaxation and after 10 and 500 fs of relaxation. Initially, the relaxation is dominated by electron-electron scattering which broadens the localized distributions according to a hot plasma temperature on a single femtosecond timescale. During this initial phase, the dynamic due to electron-phonon scatterings is about two orders of magnitude slower and, thus, irrelevant at that time. Once the carriers have relaxed into hot quasi-Fermi distributions after about 10 fs, the overall dynamic slows down by two to three orders of magnitude (see the change of units in Fig.4 from [1/fs] to [1/ps]). Here, electron-electron scattering and electron-phonon scattering become equally important. The scatterings slow further down by roughly another order of magnitude once the distributions cool down near room temperature after a few picoseconds. In- and out-scatterings due to electron-electron and electron-phonon scatterings lead eventually to the detailed balance that defines equilibrium Fermi distributions.

As can be seen in Fig.5, during the first few femtoseconds of relaxation the phonon scatterings involving acoustic phonons are of similar importance as scatterings on optical phonons. Here, the phonon scattering rates including all phonon contributions are about twice as high as when acoustical phonons are omitted. For the broadening of the initial distribution scatterings involving large momentum transfers are of particular importance. While acoustical phonons have rather limited coupling strength for small momentum transfers as they are typically involved in intra-valley relaxation, their coupling strength and energy increases with increasing momentum transfer which increase their importance for inter-valley scatter-

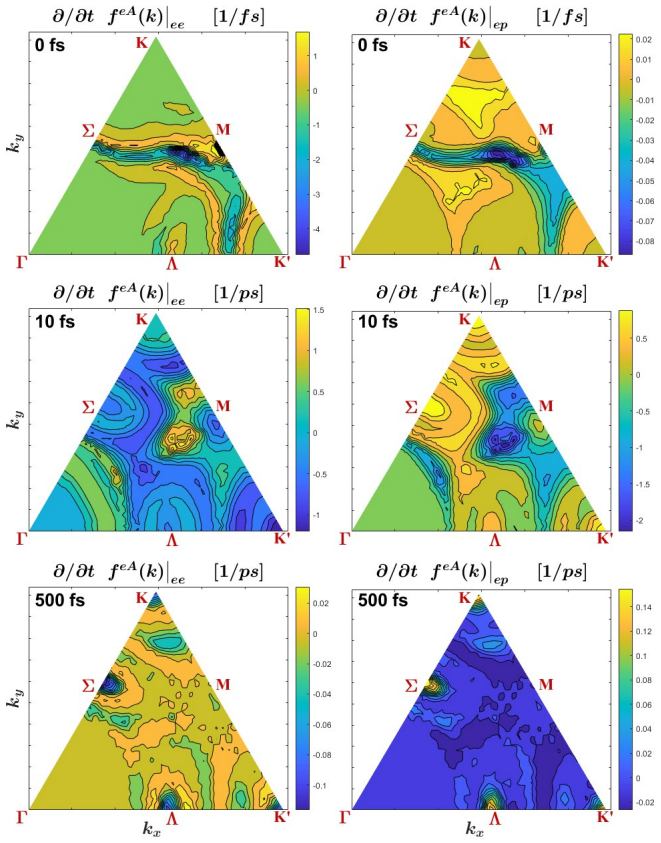

FIG. 4. Change of occupations of the electron A-band in a monolayer $MoTe_2$ at various times after initialisation as for Fig.3. Left: change due to electron-electron scattering. Right: change due to electron-phonon scattering. Units for the top two (bottom four) panels are [1/fs] ([1/ps]).

ings. Without the acoustic phonons there are only very few scatterings far from the initial distribution, like into the area between Σ, K, and M or between Σ, Λ and Γ. After the carriers have assumed a hot quasi-Fermi distribution after about 10 fs, the carrier relaxation becomes dominated by intra-valley scatterings. Here, scatterings involving optical phonons dominate the total electron-phonon interaction and the total phonon rates are almost identical to those in the absence of processes involving acoustical phonons.

For the comparison of phonon scattering contributions in Fig.5 we assumed an 8-times weaker excitation than for the results in Figs.3 and 4. Electron-electron scattering roughly scales with the density squared, while electron-phonon scattering scales about linearly with it. Thus, for this lower excitation, phonon scatterings are overall more relevant than in the earlier study. Also, it has been observed that for strong excitations the limited phonon density of states in the two-dimensional system leads to a hot phonon bottleneck[41–44]. Here, a build-up of a nonequilibrium distribution for optical phonons can strongly limit their cooling power which, in turn, increases the relative importance of acoustical phonons. This hot phonon effect is not included in our current model.

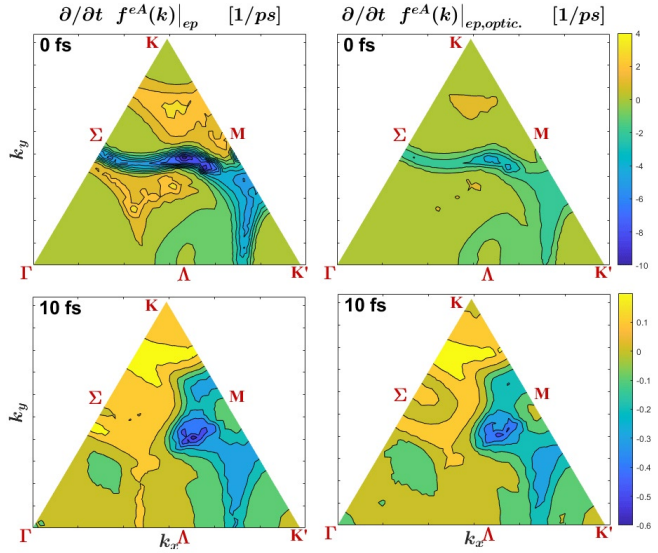

FIG. 5. Change of occupations of the electron A-band in a monolayer $MoTe_2$ due to phonon scatterings only. Top: at the beginning of carrier relaxation.Bottom: after 10 fs of relaxation. Initialisation as for Fig.3 but with $f_0 = 0.16$. Left: change due to all electron-phonon scatterings. Right: change only due to optical phonons.

2. Resonant Excitation

In order to study the inter-valley carrier transfer we place an artificial initial distribution almost exclusively in the K-valley of the A-band (and K'-valley of the B-band) and then calculate the scattering related carrier generation in the other valleys. Fig.6 shows the occupations of the electron A-band in $MoTe_2$ 2 fs after initialisation with Eq.6 resonantly at the bandgap, i.e. with $\hbar\omega_L = (\epsilon^e_{K,A} - \epsilon^h_{K,A})$, and $f_0 = 1.28$. This initialisation creates an occupation of about 0.75 at K. After the initial 2 fs of dynamics, scatterings have created electron occupations of about 0.0014 at K, 0.0003 at Σ and 0.0007 at Λ.

Electron-electron scattering leads to a very fast initial relaxation within the K-valley to establish a Fermi-like distribution there on a femtosecond timescale. However, it does not lead to significant inter-valley scattering due to the large involved momentum transfer. The rate is only about 0.1/ps for electron-electron scattering from K to K' and even less for transitions to Σ and Λ. Inter-valley transfer is dominated by electron-phonon scattering which during this initial phase creates carrier at a rate of about 0.8/ps in the K'-valley, 0.2/ps in the Λ-valley, and 0.3/ps in the Σ-valley.

Due to the much larger energy separation between the K and K' valley for holes than for electrons, the carrier

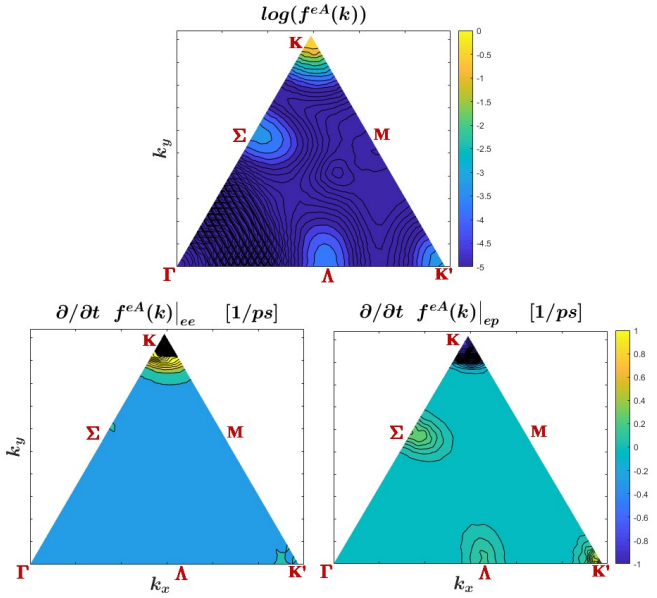

FIG. 6. Top: logarithm of the occupation of the electron A-band in a monolayer $MoTe_2$ 2 fs after initialisation with Eq.(6) resonantly at the bandgap with $f_0 = 1.28$. Bottom left: change in occupations within the electron A-band due to electron-electron scattering. Bottom right: change due to electron-phonon scattering. Grid-line spacing is 0.05/ps in the lower two figures. Please note that the solid black areas near K in the lower two graphs are due to steep slopes resulting in overlapping contour lines and not data exceeding the color bar scale.

transfer is significantly slower for these. We find a carrier generation rate at K' for holes within the A-band of only 0.004/ps for electron-electron scattering and 0.0006/ps for electron-phonon scattering,

B. Optical Excitation

After having used artificial occupations in Sec.III A in order to determine carrier relaxation timescales and the importance of underlying mechanisms, we investigate here signatures of carrier relaxation under more realistic optical excitation conditions. We excite the system with a Gaussian pulse with an envelope of $E_0 exp\left(-(t-t_0)^2/\Delta_t^2\right)$, with a width Δ_t of 50 fs. Since we are not concerned with details of the polarisation dynamics we do not evaluate the pertinent microscopic scattering processes but use a simple phenomenological dephasing rate $\hbar\gamma = 30$ meV. The central frequency of the pulse is 800 meV above the unrenormalized bandgap. While the pulse is present, carriers created by it lead to a dynamic renormalization of the bandgap[12]. As we have shown in Sec.III A, these renormalizations can be comparable to the spectral width of the 50 fs pulse. Thus, the detuning between central frequency of the pulse and the renormalized bandgap changes during the pulse which leads to an excitation that is spectrally broader than the one created by the artificial instantaneous excitation.

Fig.7 shows the occupations in the electron A-band of a monolayer of $MoTe_2$ at various times during the excitation and for two optical field strength, $E_0 = 0.0625$ MV/cm and $E_0 = 2.00$ MV/cm. These pulses create electron densities of about $1 \times 10^{11}/\text{cm}^2$ and $8 \times 10^{13}/\text{cm}^2$, respectively. For low excitation the carrier occupations stay below one percent at all times and smaller than 10^{-4} until after the center of the pulse passed. For these low occupations electron-electron scattering is very weak. Carriers remain near the original excitation until after the pulse maximum has passed and relax into the side valleys on a ten femtosecond timescale rather than the single femtosecond scale seen for higher excitation levels in Sec.III A. Some deviations from the strictly monotone energy dependence of the quasi Fermi distributions can still be seen 50 fs after the pulse maximum at the K' point.

For the strong excitation carriers relax into hot quasi-Fermi distributions already during the pulse. At the pulse maximum carriers are already predominantly relaxed to the bottom of all valleys and the only non-thermal signature is the fact that occupations at the individual valleys are not increasing with decreasing valley energy and are, e.g. higher at Λ and K' than at K. The subsequent cooling down of the carriers happens on a similar timescale as for lower excitation.

C. Energy renormalizations

In the next step, we evaluate the density dependence of the energy renormalizations for monolayers of $MoTe_2$, $MoSe_2$ and MoS_2 with carriers in global thermal equilibrium in order to check whether a transition from direct gap to indirect gap occurs. Fig.8 shows the computed renormalizations at the points K, K', Σ and Λ for these materials. At the highest densities considered here, the occupations at the K-point of the electron A-band reach reach values above 90%. For $MoTe_2$ the occupation at the highest density of $10^{14}/\text{cm}^2$ is about 95%, for $MoSe_2$ it is about 93%, and for MoS_2 the occupation at the highest density of $0.55 \times 10^{14}/\text{cm}^2$ is about 97%. We use these high percentages in order to test the extreme limits of the renormalizations, well knowing that realistic densities for technical applications such as lasers create electron occupations of only about 50% which is sufficient to generate inversion in the gain regime since the hole occupation at the K-point are usually larger due to the lack of side valleys in the hole bandstructure. To provide benchmark, we therefore mark in Fig.8 the densities at which the occupations reach the 50% level.

Alltogether, we never observe a transition to an indirect bandstructure for any of the materials investigated here. For all realistic densities, the lowest electron energy always remains at the K-point. For all materials, the change in energy with change in occupation is stronger in the Σ and Λ side valleys than at the K and K' points

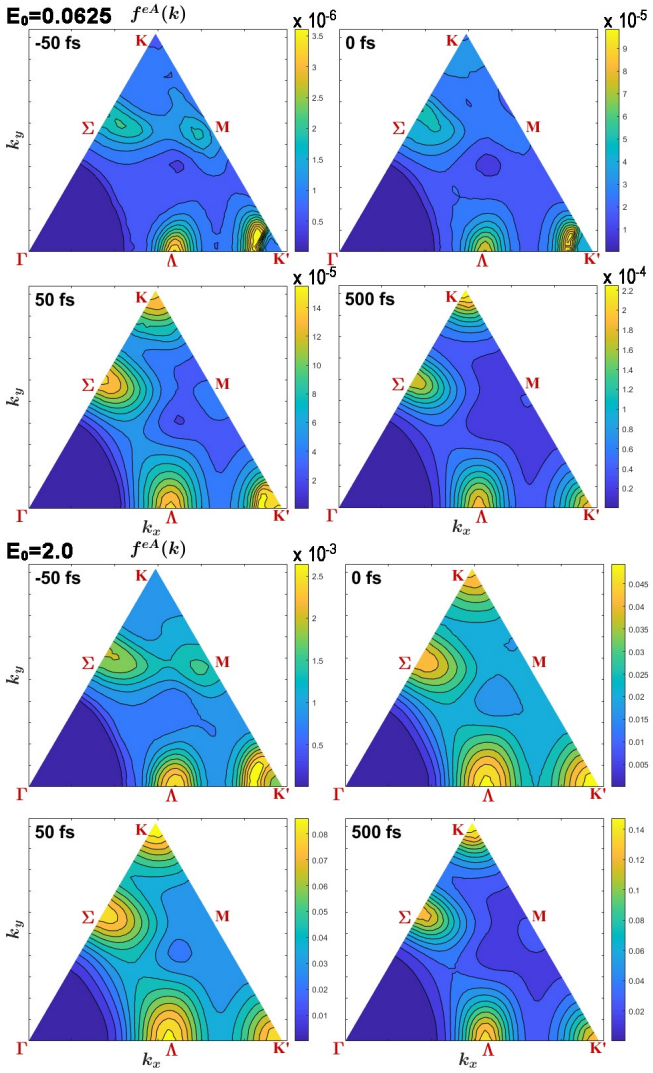

FIG. 7. Occupation of the electron A-band at various times during optical excitation with a 50 fs long Gaussian pulse. The pulse maximum is at 0 fs and the excitation energy is 800 meV above the renormalized bandgap. Top (bottom): For an optical field $E_0 = 0.0625\,\mathrm{MV/cm}$ ($E_0 = 2.00\,\mathrm{MV/cm}$).

(see the right hand side panels of Fig.8). This difference in renormalizations is caused in part by the valley dependence of the Coulomb interaction strength due to its dependence on the local wavefunction overlaps. It is also a consequence of the local bandstructure dispersion. In valleys with lower effective mass and, thus, lower density of states the occupations change stronger for a given change the in overall excitation level. However, since the side valleys are energetically significantly above the K-valley energies, their occupations in thermal equilibrium are low such that the local energy renormalizations are not strong enough to catch up to or even go below the K-point energy. Only in the hypothetical case where the energy separations in the unexcited ystems were smaller, the occupations in all valleys would be of similar order and a transition from direct to indirect would be possible.

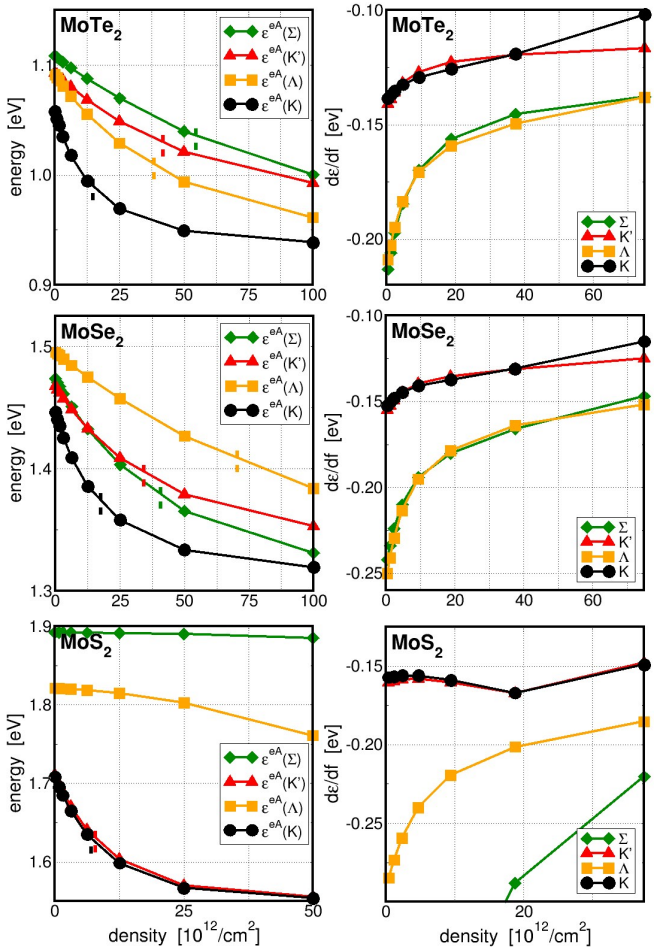

FIG. 8. Left: renormalized energies of the electron A-band at critical points in the BZ as function of the electron density for monolayers of $MoTe_2$, $MoSe_2$ and MoS_2. Short dashed vertical lines mark the density at which the occupations are 50%. Right: change of energies with increase of occupation.

The DFT determined energetic differences between the side- and the main-valley used in our work are considerably larger than those assumed in Ref.[22] where, e.g., the valley splitting at zero density in MoS_2 was assumed to be less than 15 meV while our calculations yield a separation of 113 meV (see TableI). For $MoSe_2$, we find a direct gap with a minimum valley separation of about 30 meV while Ref.[22] assumes an indirect bandgap for that material. Our determination of a direct bandgap for $MoSe_2$ agrees with most of the literature (see e.g. Refs.[45,46] and Refs. therein). Alltogether, the larger energy separations are the main reason why our calculations do not predict any transition to an indirect band configuration in contrast to the findings of Ref.[22].

IV. SUMMARY AND OUTLOOK

We combine first principle DFT calculations with fully microscopic many-body models based on the semicon-

ductor Dirac-Bloch equations in order to study the carrier dynamics and excitation induced energy renormalizations in monolayer TMDCs. Quantum Boltzmann type scattering equations for the electron-electron and electron-phonon scattering are solved taking into account the full BZ in order to resolve the detailed inter- and intra-valley relaxation processes.

For excitation high above the bandgap, we find that the carriers relax into hot quasi-Fermi distributions at the valley minima within less than 10 fs. This initial relaxation is dominated by electron-electron scatterings. For the subsequent intra-valley relaxation, electron-electron and electron-phonon scatterings turn out to be of comparable importance. The subsequent cooling of the hot plasma is mediated by phonon emission on a picosecond timescale. For resonant excitation at the K-gap, the subsequent transfer of carriers to other valleys is found to be dominated by phonon scatterings on a single picosecond timescale.

We find that non-equilibrium signatures in the electron distribution as caused by a spectrally narrow optical excitation are only observable in the low excitation regime. Electron-electron scattering processes on the same timescale of typical femtosecond pulses hide details of the excitation at higher excitation levels.

Finally, we show that for monolayer TMDCs with a direct bandgap at zero excitation and an energetic separation between the main valley and side valleys on the order of the thermal energy or more, like $MoTe_2$, $MoSe_2$ and MoS_2, the valley dependent energy renormalizations do not lead to a transition from direct to indirect bandgap. While the energy renormalization with increasing density can be stronger in the side valleys, at realistic densities it is not sufficient to shift the side-valley energetically below the K-point energy for any of the materials investigated here.

An investigation of further mono- and multi-layer TMDC materials and their heterostructures is required in order to see whether one of them allows for such a transition from direct to indirect due to smaller valley separations, and/or a significantly valley-dependent Coulomb strength and/ or density of states (effective mass). For example, an excitation induced transition from an indirect to a direct gap configuration might be possible in TMDC bi-layer systems.

DATA AVAILABILITY

All data that support the findings of this study are included within the article.

ACKNOWLEDGMENTS

The authors thank the HRZ Marburg and CSC-Goethe-HLR Frankfurt for computational resources. The Tucson work was supported by the Air Force Office of Scientific Research under award numbers FA9550-17-1-0246, FA9550-19-1-0032 and FA9550-21-1-0463..

ORCID IDS

Jörg Hader https://orcid.org/0000-0003-1760-3652
Josefine Neuhaus https://orcid.org/0000-0003-1440-1588
Jerome V. Moloney https://orcid.org/0000-0001-8866-0326
Stephan W. Koch https://orcid.org/0000-0001-5473-0170

REFERENCES

[1] Chernikov A, Berkelbach T C, Hill H M, Rigosi A, Li Y, Aslan O B, Reichman D R, Hybertsen M S and Heinz T F 2014, Exciton Binding Energy and Nonhydrogenic Rydberg Series in Monolayer WS_2, *Phys. Rev. Lett.* **113** 076802

[2] He K, Kumar N, Zhao L, Wang Z, Mak K F, Zhao H and Shan J 2014 Tightly Bound Excitons in Monolayer WSe_2 *Phys. Rev. Lett.* **113** 026803

[3] Lopez-Sanchez O, Lembke D, Kayci M, Radenovic A and Kis A 2013 Ultrasensitive Photodetectors Based on Monolayer MoS_2 *Nat. Nanotechnol.* **8** 497-501

[4] Zhang W, Huang J K, Chen C H, Chang Y H, Cheng Y J and Li L J 2013 High-Gain Phototransistors Based on a CVD MoS_2 Monolayer *Adv. Mater.* **25** 3456-61

[5] Kufer D and Konstantatos G (2015) Highly Sensitive, Encapsulated MoS_2 Photodetector with Gate Controllable Gain and Speed *Nano Lett.* **15** 7307-13

[6] Pospischil A, Furchi M M and Mueller T 2014 Solar-energy conversion and light emission in an atomic monolayer p-n diode *Nat. Nanotechnol.* **9** 257-61

[7] Sumesh C K 2019 Towards efficient photon management in nanostructured solar cells: Role of 2D layered transition metal dichalcogenide semiconductors *Solar Energy Mat. Solar Cells* **192** 16-23

[8] Sundaram R S, Engel M, Lombardo A, Krupke R, Ferrari A C, Avouris P and Steiner M 2013 Electroluminescence in single layer MoS_2 *Nano Lett.* **13** 1416-21

[9] Ross J S *et al* 2014 Electrically tunable excitonic light-emitting diodes based on monolayer WSe_2 p-n junctions *Nat. Nanotechnol.* **9** 268-72

[10] Baugher B W H, Churchill H O H, Yang Y and Jarillo-Herrero P 2014 Optoelectronic devices based on electrically tunable p-n diodes in a monolayer dichalcogenide *Nat. Nanotechnol.* **9** 262-7

[11] Lohof F, Steinhoff A, Florian M, Lorke M, Erben D, Jahnke F and Gies C 2019 Prospects and limiatations of transition metal dichalcogenide laser gain materials *Nano Lett.* **19** 210-7

[12] Meckbach L, Hader J, Huttner U, Neuhaus J, Steiner J T, Stroucken T, Moloney J V and Koch S W 2020 Ultrafast bandgap renormalization and build-up of optical gain in monolayer $MoTe_2$ *Phys. Rev. B* **101** 075401

[13] Wu S *et al* 2015 Monolayer semiconductor nanocavity lasers with ultralow thresholds *Nature* **520** 69-72

[14] Li Y, Zhang J, Huang D, Sun H, Fan F, Feng J, Wang Z and Ning C Z 2017 Room-temperature continuous-wave lasing from monolayer molybdenum ditelluride integrated with a silicon nanobeam cavity *Nat. Nanotechnol.* **12** 987-92

[15] Shang J 2017 Room-temperature 2D semiconductor activated vertical-cavity surface-emitting lasers *Nat. Commun.* **8** 543

[16]Chernikov A, Ruppert C, Hill H M, Rigosi A F and Heinz T F 2015 Population inversion and giant bandgap renormalization in atomically thin WS_2 layers *Nat. Photon.* **9** 466-70
[17]Steinhoff A, Rösner M , Jahnke F, Wehling T O and Gies C 2014 Influence of Excited Carriers on the Optical and Electronic Properties of MoS_2 *Nano Lett.* **14** 3743-8
[18]Gao S and Yang L 2017 Renormalization of the quasiparticle band gap in doped two-dimensional materials from many-body calculations *Phys. Rev. B* **96** 155410
[19]Meckbach L, Stroucken T and Koch S W 2018 Giant excitation induced bandgap renormalization in TMDC monolayers *Appl. Phys. Lett.* **112** 061104
[20]Zeng H, Dai J, Yao W, Xiao D and Cui X 2012 Valley polarization in MoS_2 monolayers by optical pumping *Nature Nanotech.* **7** 490-3
[21]Mak K F, He K, Shan J and Heinz T F 2012 Control of valley polarization in monolayer MoS_2 by optical helicity *Nature Nanotech.* **7** 494-8
[22]Erben D, Steinhoff A, Gies C, Schönhoff G, Wehling T O and Jahnke F 2018 Excitation-induced transition to indirect bandgaps in atomically thin transition-metal dichalcogenide semiconductors *Phys. Rev. B* **98** 035434
[23]Steinhoff A, Florian M, Rösner M, Lorke M, Wehling T O, Gies C and Jahnke F 2016 Nonequilibrium carrier dynamics in transition metal dichalcogenide semiconductors *2D Mater.* **3** 031006
[24]Kaasbjerg K, Thygesen K S and Jacobsen K W 2012 Phonon-limited mobility in n-type single-layer MoS_2 from first principles *Phys. Rev. B* **85** 115317
[25]Selig M, Berhäuser G, Raja A, Nagler P, Schüller C, Heinz T F, Korn T, Chernikov A, Malic E and Knorr A 2016 Excitonic linewidth and coherence lifetime in monolayer transition metal dichalcogenides *Nat. Commun.* **7** 13279
[26]Helmrich S *et al* 2021 Phonon-Assisted Intervalley Scattering Determines Ultrafast Exciton Dynamics in $MoSe_2$ Bilayers *Phys. Rev. Lett.* **127** 157403
[27]Kohn W and Sham L J 1965 Self-Consistent Equations Including Exchange and Correlation Effects *Phys. Rev.* **140** A1133-8
[28]Kresse G and Hafner J 1993 Ab initio molecular dynamics for liquid metals *Phys. Rev. B* **47** R558-61
[29]Kresse G and Hafner J 1994 Ab initio molecular-dynamics simulation of the liquid-metal amorphous-semiconductor transition in germanium *Phys. Rev. B* **49** 1425-69
[30]Kresse G and Furthmüller J 1996 Efficient iterative schemes for ab initio total-energy calculations using a plane-wave basis set *Phys. Ref. B* **54** 11169-86
[31]Kresse G and Furthmüller J 1996 Efficiency of ab-initio total energy calculations for metals and semiconductors using a plane-wave basis set *Comp. Mater. Sci.* **6** 15-50
[32]Rasmussen F A and Thygesen K S 2015 Computational 2D Materials Database: Electronic structure of Transition-Metal Dichalcogenides and Oxides *J. Phys. Chem. C* **119** 13169-83
[33]Korkmaz Y A, Bulutay C and Sevik C 2021 k·p parametrizaion and linear and circular dichroism in strained monolayer (Janus) transition metal dichalcogenides from first-principles *J. Phys. Chem. C* **125** 7439-50
[34]Blundo E, Felici M, Yildirim T, Pettinati G, Tedeschi D, Miriametro A, Liu B, Ma W, Lu Y, and Polimeni A 2020 Evidence of the direct-to-indirect band gap transition in strained two-dimensional WS_2, MoS_2, and WSe_2 *Phys. Rev. Research* **2** 012024(R)
[35]Zhang C, Chen Y, Johnson A, Li M-Y, Li L-J, Mende P C, Feenstra R M and Shih C-K 2015 Probing critical point energies of transition metal dichalcogenides: Surprising indirect gap of single layer WSe_2 *Nano Lett.* **15** 6494-500
[36]Giannozzi P *et al* 2009 QUANTUM ESPRESSO: a modular and open-source software project for quantum simulations of materials *J. Phys.: Condens. Matter* **21** 395502
[37]Giannozzi P *et al* 2017 Advanced capabilities for materials modelling with QUANTUM ESPRESSO *J. Phys.: Condens. Matter* **29** 465901
[38]Kormányos A, Burkard G, Gimtra M, Fabian J, Zólyomi V, Drummond N D and Fal'ko V 2015 k·p theory for two-dimensional transition metal dichalcogenide semiconductors *2D Mater.* **2** 022001
[39]Shafique A and Shin Y-H 2017 Strain engineering of phonon thermal transport properties in monolayer 2H-$MoTe_2$ *Phys. Chem. Chem. Phys.* **19** 32072-8
[40]Zulfiqar M, Zhao Y, Li G, Li Z C and Ni J 2019 Intrinsic Thermal conductivities of monolayer transition metal dichalcogenides MX_2 (M=Mo, W; X=S, Se, Te) *Sci. Rep.* **9** 4571
[41]Kaasbjerg K, Bhargavi K S and Kubakaddi S S 2014 Hot-electron cooling by acoustic and optical phonons in monolayers of MoS_2 and other transition-metal dichalcogenides *Phys. Rev. B* **90** 165436
[42]Nie Z, Long R, Teguh J S, Huang C-C, Hewak D W, Yeow E K L, Shen Z, Prezhdo O V and Loh Z-H 2015 Ultrafast Electron and Hole Relaxation Pathways in Few-Layer MoS_2 *J. Phys. Chem. C* **119** 20698-708
[43]Shah J, Pinczuk A, Gossard A C and Wiegmann W 1985 Energy-Loss Rates for Hot Electrons and Holes in GaAs Quantum Wells *Phys. Rev. Lett.* **54** 2045-8
[44]Breusing M, Kuehn S, Winzer T, Mali'c E, Milde F, Severin N, Rabe J P, Ropers C, Knorr A and Elsaesser T 2011 Ultrafast Nonequilibrium Carrier Dynamics in a Single Graphene Layer *Phys. Rev. B: Condens. Matter Mater. Phys.* **83** 153410
[45]Pandey S K, Das R and Mahadevan P 2020 Layer-Dependent Electronic Structure Changes in Transition Metal Dichalcogenides: The Microscopic Origin *ACS Omega* **5** 15169-76
[46]Silva-Guillén J A, San-Jose P and Roldán R 2016 Electronic Band Structure of Transition Metal Dichalcogenides from Ab Initio and Slater-Koster Tight-Binding Model *Appl. Sci.* **6** 284